NURBS-enriched contact finite elements

Callum J. Corbett, Roger A. Sauer[1]

Aachen Institute for Advanced Study in Computational Engineering Science (AICES), RWTH Aachen University, Templergraben 55, 52056 Aachen, Germany

Accepted for publication[2] in *Computer Methods in Applied Mechanics and Engineering*,
DOI: 10.1016/j.cma.2014.02.019
Submitted on 14. March 2013, Revised on 20. February 2014, Accepted on 27. February 2014

Abstract

A novel enrichment of finite elements for contact computations based on isogeometric analysis is presented. Each body is divided into two parts, an enriched contact surface and the bulk domain together with surfaces that are not in contact. The latter part comprises the large majority of the domain and is treated in the usual manner with standard linear basis function, preserving the efficiency of classical finite element techniques. The enriched contact surface is discretized using NURBS basis functions of at least second order, allowing for a locally differentiable surface representation. This avoids the problem of suddenly changing normal vectors between element boundaries on the contact surface. Following the concept of isogeometric analysis, the smooth basis functions are not only used to describe the surface geometry, but also to approximate the solution on the surface. This leads to higher accuracy in the contact integral evaluation.
Numerical results are presented for 2D and 3D contact computations including frictionless sliding, adhesive peeling, and cohesive debonding. The presented contact element enrichment exhibits a major gain in numerical accuracy and stability without loss of efficiency compared to standard linear finite elements. The enrichment technique offers some advantages over Hermite and higher-order Lagrangian contact element enrichment techniques, such as locally differentiable surface representations in 3D, while featuring competitive accuracy and performance.

Keywords: computational contact mechanics, isogeometric analysis, nonlinear finite element methods, cohesive zone modeling, sliding, peeling

1 Introduction

This work presents a novel local finite element enrichment technique for contact computations that is both accurate and efficient. Computational contact of deformable solids plays an important role in engineering problems. Due to the complex nature of contact problems, numerical methods are often the only feasible approach to solve them. Efficient and highly accurate methods are therefore needed in research and industry alike.
The presented formulation combines the high accuracy achieved with isogeometric analysis with the efficiency of classical linear finite elements. The contact surface is locally enriched with NURBS-based isogeometric surface elements, while the bulk is discretized with linear elements. By using the enrichment for both, geometry and analysis, this leads to an accurate and continuous contact surface description and a higher accuracy in the contact integral evaluation. An at least C^1-continuous surface implies a continuous normal vector on the surface, making

[1]corresponding author, email: sauer@aices.rwth-aachen.de

the projection of points to this surface simpler and more robust. The NURBS enrichment offers a viable alternative to using highly refined meshes, as it provides highly accurate results on comparably coarse meshes. It is shown that the use of NURBS enriched elements can even decrease the runtime of contact computations compared to standard linear elements due to faster convergence of the solver.

Isogeometric analysis (IGA) was first introduced by [Hughes et al. (2005)] and is summarized in [Cottrell et al. (2009)]. NURBS, the CAD modeling standard, are used as basis functions for finite elements. Recent advances include the introduction of the Bézier extraction operator [Borden et al. (2011)], allowing IGA to be embedded conveniently into existing finite element codes by supplying a familiar element based representation. The extension to T-splines by [Bazilevs et al. (2010)] offers the possibility of local mesh refinement.

A summary of non-linear computational contact mechanics is given in [Laursen (2002)] and [Wriggers (2006)]. The use of IGA in contact computations has been investigated recently by [De Lorenzis et al. (2011)], [Lu (2011)], [De Lorenzis et al. (2012)], and [Temizer et al. (2012))], and includes 2D and 3D, frictional and frictionless problems solved with various methods to describe and enforce the contact conditions, like mortar methods and the augmented Lagrangian method. In these papers the entire geometry is discretized with NURBS, as opposed to only discretizing the contact surface as proposed in this work.

An approach used to obtain continuous normal vectors on a C^0 facet-based contact surface is geometrical contact smoothing. Various techniques exist to obtain a locally at least C^1-continuous surface. These techniques use Hermite ([Padmanabhan and Laursen (2001)]), Bézier ([Krstulovic-Opara et al. (2002)]), Spline ([El-Abbasi et al. (2001)]), or NURBS ([Stadler et al. (2003)]) interpolation to approximate the contact surface. More recently, subdivision surfaces have also been used as a smoothing technique in [Stadler and Holzapfel (2004)]. While these formulations provide a continuous normal vector across element boundaries, the surface integrals are still approximated linearly. Also, consistent linearization of the contact terms becomes increasingly complex due to the influence of neighboring elements in the smoothing terms. The presented formulation provides a smooth surface representation without applying further smoothing techniques. The use of the NURBS basis functions to evaluate the surface integrals provides a higher-order approximation of these terms. Consistent linearization of the surface integrals then only depends on the two elements in contact.

Finite elements with one curved surface go back to [Zlámal (1973)], [Scott (1973)], and [Gordon and Charles (1973)]. They rely on a mapping of linear elements to a curved boundary. More recently the NURBS-Enhanced Finite Element Method (NEFEM) was proposed by [Sevilla et al. (2008)]. It maps Lagrangian elements to a surface defined by NURBS and uses an adapted integration rule to take into account the curved boundary. Besides the low-order integration on the curved boundary, the NURBS surface is also considered rigid. Deforming the NURBS surface during computation, essential for computational contact, requires fitting the NURBS surface in each step. In the presented formulation, the displacement degrees of freedom are solved directly on the NURBS control points. The deformation of the surface is thus obtained automatically.

Previously proposed surface enrichments contain higher-order Lagrangian and Hermite interpolation, [Sauer (2011)] and [Sauer (2013)], which both yield good results in contact computations. Though Hermite interpolation on the surface also results in a C^1-continuous surface representation, it lacks an extension to 3D. Lagrangian enrichment is possible in 2D and 3D, but C^0-continuity across element boundaries remains. The NURBS-enrichment yields C^1-continuity and higher in 2D and 3D.

The following section gives a brief overview of the computational contact models used in this paper and a summary of isogeometric analysis. Section 3 presents the NURBS-enriched contact elements and related refinement strategies. Numerical examples are discussed in section 4. The

results for NURBS-enriched contact elements are compared to those of standard linear finite elements and Lagrangian and Hermite enriched contact elements. Section 5 concludes the paper.

2 Preliminaries

This section gives a very brief overview of the non-linear finite element method, computational contact, and isogeometric analysis. The following theory is applicable in $\mathbb{R}^d$ with $d = 2, 3$, but for simplicity isogeometric analysis is presented for NURBS curves only.

2.1 Computational contact in the framework of non-linear finite elements

Consider two bodies $\mathcal{B}_k$ $(k = 1, 2)$ with surfaces $\partial\mathcal{B}_k$. Parts of these surfaces, $\partial_c\mathcal{B}_k$, can come into contact with one another. The weak form for quasi-static contact describes the equilibrium between internal and external virtual work and the virtual contact work acting between the bodies. In the examples to follow, the two-half-pass contact algorithm from [Sauer and De Lorenzis (2013)] will be used to compute the contact tractions whenever two deformable bodies are considered. It evaluates the contact traction $\boldsymbol{t}_{ck}$ on each surface $\partial_c\mathcal{B}_k$ separately. In contrast, traditional one-pass algorithms evaluate the contact tractions $\boldsymbol{t}_{ck}$ on the slave surface $\partial_c\mathcal{B}_k$ and apply $-\boldsymbol{t}_{ck}$ to the master surface $\partial_c\mathcal{B}_\ell$. This creates a bias in the formulation and involves the integration of neighboring surface quantities, two drawbacks that are avoided by the two-half-pass algorithm. Traditional one-pass algorithms do however satisfy the local balance of linear momentum in the discrete setting a priori. The two-half-pass contact algorithm does not enforce local satisfaction of linear momentum in the discrete setting, but it is satisfied exactly in the continuum setting. It follows, that the discrete approximation satisfies local linear momentum to high accuracy and converges with mesh refinement.
Using the two-half-pass algorithm, the task is to find the mechanical deformation field $\boldsymbol{\varphi}_k \in \mathcal{U}_k$ satisfying the weak form

$$\sum_{k=1}^{2}\left[\int_{\mathcal{B}_k} \operatorname{grad}(\delta\boldsymbol{\varphi}_k) : \boldsymbol{\sigma}_k \, \mathrm{d}v_k \underbrace{- \int_{\partial_c\mathcal{B}_k} \delta\boldsymbol{\varphi}_k \cdot \boldsymbol{t}_{ck} \, \mathrm{d}a_k}_{\text{virtual contact work}} - \delta\Pi_{\text{ext},k}\right] = 0 \;, \quad \forall\, \delta\boldsymbol{\varphi}_k \in \mathcal{V}_k \tag{1}$$

for the two-body system, where $\mathcal{U}_k$ is the space of kinematically admissible deformations. Within equation (1), $\boldsymbol{\sigma}_k$ is the Cauchy stress tensor, $\boldsymbol{t}_k$ is the contact traction on surface $\partial_c\mathcal{B}_k$, $\delta\Pi_{\text{ext},k}$ is the external virtual work, and $\mathcal{V}_k$ is the space of kinematically admissible variations.
The finite element approximation of the weak form (1) is obtained by discretization of the volume to a set of elements Ω_k^e with n^e nodes such that $\mathcal{B}_k \approx \mathcal{B}_k^h = \bigcup_e \Omega_k^e$, and a set of surface elements Γ_k^e with n_s^e nodes such that $\partial\mathcal{B}_k \approx \partial\mathcal{B}_k^h = \bigcup_e \Gamma_k^e$. Approximated quantities are assigned the index h. With the basis functions $N_1, \ldots, N_{n^e}$ the displacement field $\boldsymbol{u}_k$ within an element Ω_k^e is then interpolated as

$$\boldsymbol{u}_k \approx \boldsymbol{u}_k^h = \mathbf{N}_k \mathbf{u}_k^e \tag{2}$$

with $\mathbf{N}_k = \left[\, N_1 \boldsymbol{I} \,,\; N_2 \boldsymbol{I} \,,\; \ldots \,,\; N_{n^e} \boldsymbol{I} \,\right]$, the identity tensor $\boldsymbol{I}$ in $\mathbb{R}^d$, and the nodal displacements of the element $\mathbf{u}_k^e$. Continuous quantities are printed in italics while discretized quantities are printed roman. The virtual displacement field $\delta\boldsymbol{\varphi}_k \approx \boldsymbol{v}_k^h$, the deformation field $\boldsymbol{x}_k \approx \boldsymbol{x}_k^h$, and the reference configuration $\boldsymbol{X}_k \approx \boldsymbol{X}_k^h$ are interpolated likewise.
With this interpolation, the discretized weak form can be written as

$$\mathbf{v}^T\left[\mathbf{f}_{\text{int}} + \mathbf{f}_{\text{c}} - \mathbf{f}_{\text{ext}}\right] = 0 \quad \forall\, \mathbf{v} \in \mathcal{V}_h \tag{3}$$

with internal forces $\mathbf{f}_{\text{int}}$, contact forces $\mathbf{f}_{\text{c}}$, and external forces $\mathbf{f}_{\text{ext}}$.

The contact contribution of an element Ω_k^e can be computed as the integral over the element surface in the reference configuration Γ_{0k}^e or in the current configuration Γ_k^e,

$$\mathbf{f}_{ck}^e = -\int_{\Gamma_{0k}^e} \mathbf{N}_k^T \boldsymbol{T}_{ck} \, \mathrm{d}A = -\int_{\Gamma_k^e} \mathbf{N}_k^T \boldsymbol{t}_{ck} \, \mathrm{d}a \; . \tag{4}$$

In the examples to follow, the traction $\boldsymbol{T}_{ck}$ or $\boldsymbol{t}_{ck}$ is given through the penalty method and contact constitutive laws for adhesion and cohesion. In all cases, the traction depends on the gap $\boldsymbol{g}$, the surface normal at the projection point $\boldsymbol{n}_{\text{p}}$, and parameters of the contact model. The gap $\boldsymbol{g} = \boldsymbol{x}_k - \boldsymbol{x}_{\text{p}}$ is the distance between the point $\boldsymbol{x}_k$ on surface $\partial_{\text{c}}\mathcal{B}_k$ and its projection point $\boldsymbol{x}_{\text{p}}$ on the neighboring body. The normal gap is defined as $g_{\text{n}} = (\boldsymbol{x}_k - \boldsymbol{x}_{\text{p}}) \cdot \boldsymbol{n}_{\text{p}}$ and is positive if there is a gap between the bodies, and negative if the bodies are penetrating.
The penalty method

$$\boldsymbol{t}_{ck}(\boldsymbol{x}_{\text{s}}) = \begin{cases} -\varepsilon_{\text{n}} \, g_{\text{n}} \, \boldsymbol{n}_{\text{p}} \; , & g_{\text{n}} < 0 \\ 0 \; , & g_{\text{n}} \geq 0 \end{cases} \tag{5}$$

applies a traction in normal direction, which is proportional to the penetration depth. The proportionality constant is the penalty parameter ε_{n}.
Van der Waals adhesion is described by

$$\boldsymbol{T}_{ck}(\boldsymbol{x}_{\text{s}}) = T_{\text{c}} \, \boldsymbol{n}_{\text{p}} \; , \qquad T_{\text{c}}(r_{\text{s}}) = \frac{A_{\text{H}}}{2\pi r_0^3} \left[\frac{1}{45} \left(\frac{r_0}{\|\boldsymbol{g}\|} \right)^9 - \frac{1}{3} \left(\frac{r_0}{\|\boldsymbol{g}\|} \right)^3 \right] \; , \tag{6}$$

with the Hamaker's constant A_{H} and the atomic equilibrium spacing of the Lennard-Jones potential r_0. This formulation for adhesive contact is taken from [Sauer (2011)], where details can be found.
The exponential cohesive zone model

$$\boldsymbol{T}_{ck}(\boldsymbol{x}_{\text{s}}) = -T_0 \, \frac{\|\boldsymbol{g}^0\|}{g_0} \, \exp\left(1 - \frac{\|\boldsymbol{g}^0\|}{g_0}\right) \, \frac{\boldsymbol{g}^0}{\|\boldsymbol{g}^0\|} \tag{7}$$

depends on the gap $\boldsymbol{g}^0$ and the parameters T_0 and g_0. In the reference configuration, the projection point $\boldsymbol{X}_p^0$ is computed for each surface point $\boldsymbol{X}_k$. The gap $\boldsymbol{g}^0$ is the gap between the current surface point $\boldsymbol{x}_k$ and the current position $\boldsymbol{x}_p^0$ of the original projection point $\boldsymbol{X}_p^0$. This model is a special case of the cohesive zone model by [Xu and Needleman (1993)], as it is used in [Sauer (2013)].

2.2 Isogeometric analysis

A brief review of isogeometric analysis with NURBS is given. For simplicity, only NURBS curves are considered here, the extension to NURBS surfaces is straightforward due to their tensor-product structure, see [Piegl and Tiller (1997)]. We will refer to piecewise linear, quadratic, cubic etc. polynomials as curves of *order* $p = 1, 2, 3, \ldots$. This convention was proposed by [Hughes et al. (2005)] to maintain the usual terminology in finite element literature. In the computational geometry community this is usually referred to as *degree*.
A NURBS curve is based on a B-spline curve, which is defined by its order, control points, and knot vector. In general, a B-spline curve of order p is C^{p-1} continuous, which makes the cases $p = 2$ and $p = 3$ especially interesting for contact computations. The quadratic case offers

continuous surface normals, the cubic case additionally a continuous curvature. The control points are a set of n vector valued points

$$\mathbf{P} = \{\mathbf{P}_A\}_{A=1}^{n}, \text{ with each } \mathbf{P}_A \in \mathbb{R}^d \ . \tag{8}$$

The convex hull of the polygon spanned by $\mathbf{P}$ completely contains the B-spline curve. The knot vector is a set of non-decreasing parametric coordinates

$$\boldsymbol{\Xi} = \{\xi_1, \xi_2, \ldots, \xi_{n+p+1}\} \ . \tag{9}$$

Each unique knot value determines the position ξ at which the pieces of curves are connected. The first and last knot value are repeated $p+1$ times which makes the curve interpolatory at its ends. Knot vectors with this property are referred to as open knot vectors. Repeated interior knot values lead to a reduction of continuity at the repeated knot value. A knot with multiplicity m reduces the continuity to C^{p-m}. With the order p and the knot vector $\boldsymbol{\Xi}$, the set of B-spline basis functions $\hat{\mathbf{N}}_p = \{\hat{N}_{A,p}\}_{A=1}^{n}$ is defined as

$$\hat{N}_{A,p}(\xi) = \frac{\xi - \xi_A}{\xi_{A+p} - \xi_A}\hat{N}_{A,p-1}(\xi) + \frac{\xi_{A+p+1} - \xi}{\xi_{A+p+1} - \xi_{A+1}}\hat{N}_{A+1,p-1}(\xi) \ , \quad \text{for } p > 0 \tag{10}$$

with

$$\hat{N}_{A,0}(\xi) = \begin{cases} 1 \ , & \text{if } \xi_A \leq \xi < \xi_{A+1} \\ 0 \ , & \text{otherwise} \end{cases} \ . \tag{11}$$

To go from a B-spline curve to a NURBS curve, the weights w_B, assigned to each control point, and the weighting function

$$W(\xi) = \sum_{B=1}^{n} w_B \, \hat{N}_{B,p}(\xi) \tag{12}$$

are needed. Together with the B-spline basis, the weights and the weighting function define n rational basis functions

$$R_{A,p}(\xi) = \frac{w_A \hat{N}_{A,p}(\xi)}{W(\xi)} \ , \quad A = 1 \ldots n \tag{13}$$

for NURBS curves. Introducing the diagonal matrix of weights $\mathbf{W}$ and dropping the index p, equation (13) can be written in matrix form for the set of basis functions $\mathbf{R}(\xi) = \{R_{A,p}(\xi)\}_{A=1}^{n}$

$$\mathbf{R}(\xi) = \frac{\mathbf{W}\hat{\mathbf{N}}(\xi)}{W(\xi)} \ . \tag{14}$$

A point $\mathbf{S}(\xi)$ on the NURBS curve is given by

$$\mathbf{S}(\xi) = \sum_{A=1}^{n} \mathbf{P}_A \, R_{A,p}(\xi) = \mathbf{P}^{\mathrm{T}} \, \mathbf{R}(\xi) \ , \quad \xi \in [\xi_1, \xi_{n+p+1}] \ . \tag{15}$$

To use the rational NURBS basis in finite element computations, it is convenient to make use of the Bézier extraction operator introduced by [Borden et al. (2011)]. The localized Bézier extraction operator $\mathbf{C}^e$ allows the numerical integration of the continuous rational basis functions to be performed on C^0 Bézier elements with a set of $p+1$ Bernstein polynomials $\mathbf{B}^e$ as basis functions local to one element Γ^e. For all elements of order p the set $\mathbf{B}^e$ is identical, the information about the smoothness is shifted to the linear operator $\mathbf{C}^e$ that is in general different for each element but needs to be computed only once. Written in matrix form, the rational shape functions $\mathbf{R}^e$ of an element can then be computed by

$$\mathbf{R}^e(\xi) = \frac{\mathbf{W}^e\mathbf{C}^e\mathbf{B}^e(\xi)}{W(\xi)} \ , \quad \xi \in [-1, 1] \tag{16}$$

where the B-spline basis function evaluations are replaced by the evaluation of Bernstein polynomials and a matrix product $\mathbf{C}^e\mathbf{B}^e(\xi)$. This substitution is also used to evaluate the weighting function $W(\xi)$. The diagonal matrix $\mathbf{W}^e$ contains the weights associated to the control points of the element. The Bézier extraction operator provides a familiar, element-based finite element structure as opposed to the patch-level structure intrinsic to NURBS.
NURBS surface basis functions are defined by the tensor product of univariate 1D NURBS basis functions. The Bézier extraction operator and the following refinement strategies can be applied to NURBS surfaces in a straightforward manner.

2.2.1 Refinement strategies

Refinement of NURBS curves can be done in two different manners, by means of knot insertion and order elevation. The first, knot insertion, is equivalent to classical h-refinement. Inserting a new, unique knot value into the knot vector leads to an additional knot-span and consequently an additional Bézier element. The geometry and parameterization of the curve remain unchanged by knot insertion, as does the continuity for unique knot values. As stated above, repeating knot values decreases the continuity.
Order elevation is analogue to classical p-refinement. The order of the basis can be elevated t times from p to $p+t$, again without changing the geometry or parameterization of the curve. Each unique knot value must be repeated t times in this procedure, which implies that the continuity across existing element boundaries is not raised during order elevation.
The fact that knot insertion and order elevation do not commute is used in [Hughes et al. (2005)] to introduce k-refinement. When applying k-refinement, the curve's order is first elevated from order p to order $q = p + t$, followed by knot insertion to the desired discretization. This order creates new elements by knot insertion which are $q - 1$ continuous. If the order of refinements were reversed and knot insertion performed first, the continuity of these new elements would be $p - 1$ and remain that way during order elevation, as unique knot values are repeated during this procedure.
In section 3.3, an alternative refinement strategy for the NURBS-enriched contact finite elements is proposed.

3 Enriched contact finite elements

NURBS-enriched contact finite elements are introduced in this section, followed by the discussion of the treatment of contact contributions and mesh refinement strategies for these elements. Some remarks on numerical integration and the integration of the enrichment technique into existing code are given. A brief review of Lagrangian and Hermite element enrichment, which the NURBS enrichment is compared to in the numerical examples, concludes the section.

3.1 Finite element interpolation

For simplicity the theory is presented for the two-dimensional case, the extension to 3D is discussed briefly at the end of this section. Here, the term *node* refers to both standard finite element nodes and control points of the NURBS curve. Consider a body $\mathcal{B}$ with contact surface $\partial_c\mathcal{B}$. The discretized contact surface $\partial_c\mathcal{B}^h$ is given by a NURBS curve of order p. The bulk of the body and surfaces other than the contact surface are discretized with standard linear finite elements. Thus, the layer of elements on the contact surface have one face represented by the NURBS curve and three linear faces. Such an element is defined by $n^e = p + 3$ nodes, $p + 1$ on

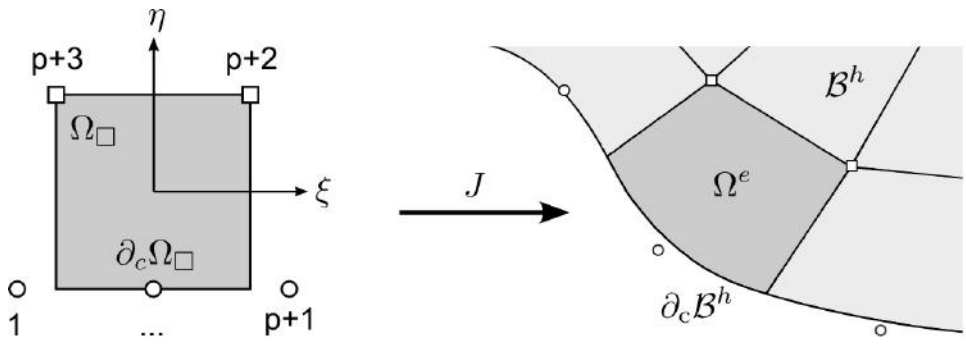

Figure 1: Schematic sketch of the 2D Q1Np master element $\Omega_\square$ and its current configuration Ω^e. Control points of the NURBS curve are depicted as circles, standard finite elements nodes as squares.

the NURBS surface and 2 in the interior domain, see Figure 1. Without loss of generality, the surface $\eta = -1$ of the master element $\Omega_\square$ is considered to be enriched. The basis functions of such an element are

$$\begin{aligned} N_1 &= R^e_1(\xi)\,\tfrac{1}{2}(1-\eta) \\ &\vdots \\ N_{p+1} &= R^e_{p+1}(\xi)\,\tfrac{1}{2}(1-\eta) \\ N_{p+2} &= \tfrac{1}{4}(1+\xi)(1+\eta) \\ N_{p+3} &= \tfrac{1}{4}(1-\xi)(1+\eta) \end{aligned} \tag{17}$$

with the rational basis functions R^e_i defined in equation (16), using the Bézier extraction operator. They form a partition of unity

$$\sum_{i=1}^{p+3} N_i(\xi,\eta) = 1 \quad \forall \xi,\eta \in \Omega_\square \tag{18}$$

and are greater or equal to zero on the contact surface

$$N_i(\xi,-1) \geq 0 \quad \forall \xi \in \Gamma_\square, \quad i = 1,\dots,p+1\,. \tag{19}$$

The NURBS-enriched element is denoted Q1Np, where p is the order of the NURBS curve.

The basis functions (17) are used for the geometry in the initial and current configuration and for analysis to approximate the solution

$$\boldsymbol{u}^e \approx \mathbf{u}^e = \textstyle\sum_{i=1}^{n^e} N_i\,\mathbf{u}_i\,. \tag{20}$$

This results not only in a continuous normal vector used in finding the closest point projection on the contact surface, but also in higher-order integration of the contact traction.
Setting the order $p = 1$ and all weights to 1, the NURBS basis functions are equal to standard linear basis functions. Thus, standard bi-linear Lagrange elements, denoted Q1C1, are contained in this formulation as the special case Q1N1.
For a three dimensional body, the surface is enriched by a NURBS surface of order p and q. One element then consists of $n^e = (p+1)(q+1)+4$ nodes, $(p+1)(q+1)$ on the contact surface and four in the bulk domain. The basis functions and approximations follow in an analogous manner. In the three-dimensional example in 4.4 we set $p = q$ and maintain the short notation Q1Np.

3.2 Contact contributions

For the computation of the contact contribution, only the contact surface $\partial_c\mathcal{B}$ is necessary. The discretized contact surface $\partial_c\mathcal{B}^h$ is the NURBS curve or surface, inherited directly from the Q1Np elements. All contact computations rely on the projection of a surface point on one body to another, or itself in the case of self-contact which is not considered here. The advantage of a surface representation that is C^1 continuous or higher, is the continuity of the normal vector across element boundaries. Two deformable bodies moving tangentially to each other with respect to their surfaces cause projection points of one surface to move across element boundaries on the neighboring surface. Using C^0 surface elements results in sudden changes of the normal vector between elements, in which case an orthogonal projection point may not exist and a projection to an element edge or corner must be considered. This drawback is avoided with a smooth surface formulation. Figure 2 illustrates the projection of point $\boldsymbol{x}_k$ to the contact surface $\partial_c\mathcal{B}^h$. The continuous surface representation on the left leads to a projection point $\boldsymbol{x}_\mathrm{p}$ at which the direction of the surface normal $\boldsymbol{n}_\mathrm{p}$ coincides with the direction of the normal gap g_n. On the right, the same surface is discretized using linear elements. No orthogonal projection in direction of the surface normals $\boldsymbol{n}_1$ or $\boldsymbol{n}_2$ exists, the closest point projection $\boldsymbol{x}_\mathrm{p}$ is the element corner at which a "normal vector" must be defined, for instance coinciding with the direction along the gap g_n or as average of $\boldsymbol{n}_1$ and $\boldsymbol{n}_2$. Multiple projection points may still exist with Q1Np elements and at actual C^0 edges or corners a projection to these geometric features is still necessary.

The projection algorithm can take advantage of the continuous surface representation $\partial_c\mathcal{B}^h$ when projecting a point $\boldsymbol{x}_k$ onto it. Assuming the relative movement of the bodies is sufficiently small, the local surface coordinates $(\xi^1_{p^{n-1}}, \xi^2_{p^{n-1}})$ of the projection point of the last iteration $\boldsymbol{x}^{n-1}_\mathrm{p}$ are a good initial guess for the new projection point of $\boldsymbol{x}^n_k$, which is computed with a Newton algorithm. If one or both of the local surface coordinates exceed the domain of the element $\Omega_\square$ during the Newton iteration, the coordinates are converted to the local coordinate system of the neighboring element. This leads to a good starting point on the new element under the mild condition that the elements on $\partial_c\mathcal{B}^h$ are of similar size.
An additional advantage of the formulation is that algorithms developed for the NURBS-enriched surface, like a contact algorithm, can be used directly for computations involving only the surface like NURBS-based shell and membrane computations.

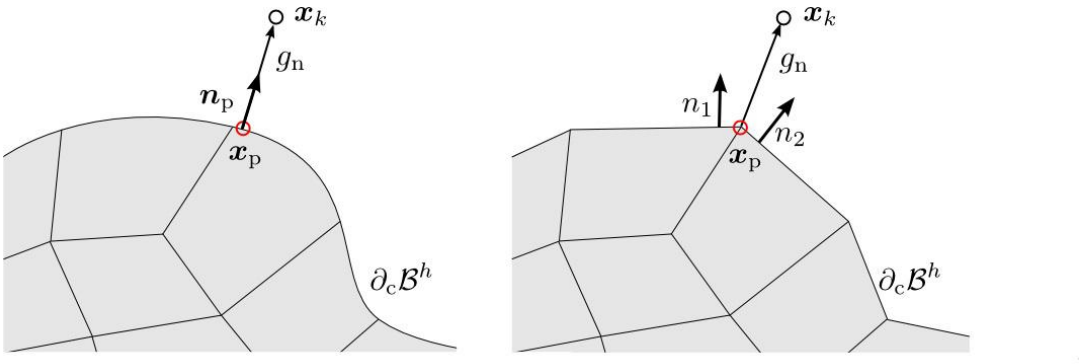

Figure 2: Projection of point $\boldsymbol{x}_k$ to surface $\partial_c\mathcal{B}^h$ with a smooth surface (left) and a faceted surface (right)

3.3 Alternative refinement strategy

In section 2.2, h-, p-, and k-refinement are discussed. Here, an alternative surface-oriented refinement strategy is introduced. In computational contact computations, k-refinement does not lead to the best results, as section 4 discusses. The increased continuity is directly linked to an increase of the basis function support. Very smooth basis functions are not capable of accurately capturing the contact line, since the sharp transition from contact to no contact is smoothed. Also, as illustrated in the left column of Figure 3, control points agglomerate along the patch edges and points (1D) or lines (2D) of reduced continuity. The half sphere in Figure 3 has a C^1 continuous point at its lowest point throughout all meshes due to the starting mesh of order $p = 2$ consisting of two Bézier elements. Between the control point agglomerations, the control points are sparsely spaced with one element length L_e between them, regardless of the order p. In general, only part of the contact surface $\partial_c \mathcal{B}^h$ is in contact, leading to few degrees of freedom in the actual contact zone.

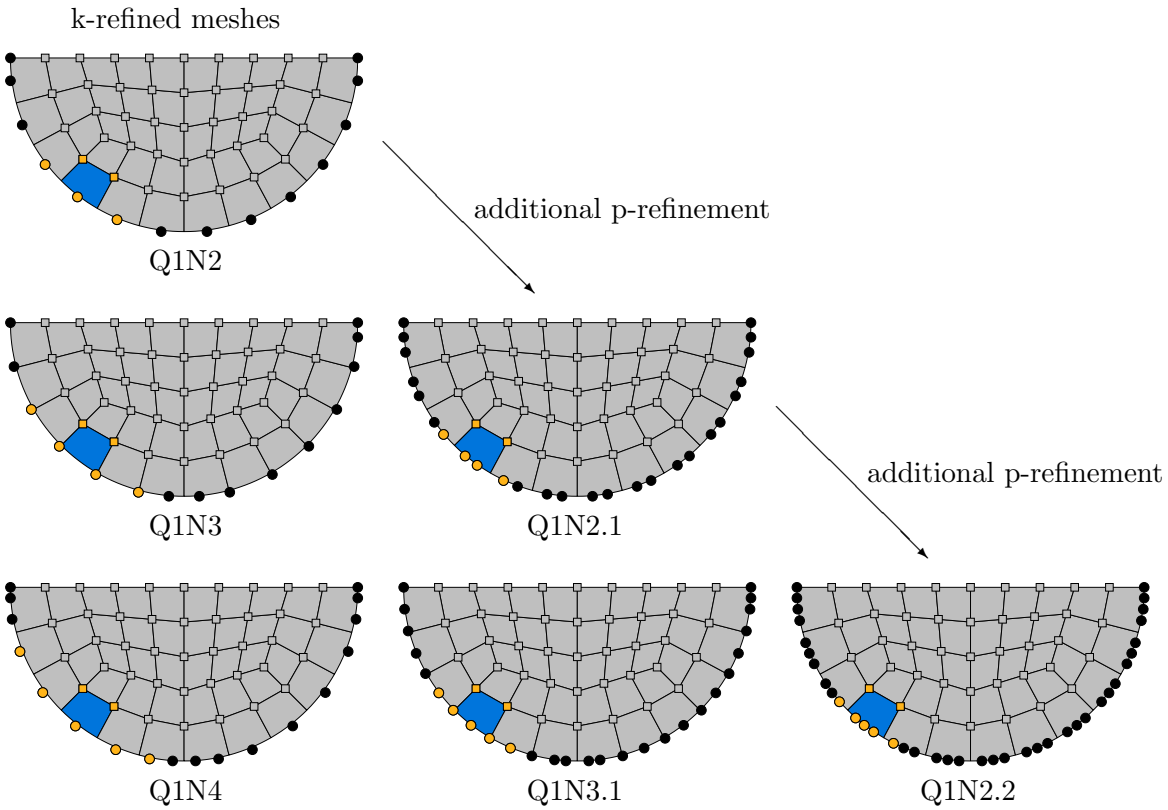

Figure 3: Different refinement strategies for NURBS-based surface enrichment. One NURBS-enriched element is highlighted with its nodes on each mesh. The NURBS control points are depicted as circles, standard finite element nodes as squares.

An alternative refinement strategy is proposed here, following the k-refinement with additional p-refinement. The order elevation during k-refinement should thereby only be performed to the necessary continuity. For contact computations, quadratic or cubic basis functions are considered sufficient. Then, the desired element size and number is obtained with knot insertion. This k-refinement leads to a mesh like in the left column of Figure 3, where one NURBS-enriched element has been highlighted with its nodes on each mesh to visualize the differences between

Elements	surface continuity	# DOF	n_s^e	node span in L_e	n_{ex}	n_{max}
Q1N2	C^1	10	3	2	0	3
Q1N3	C^2	12	4	3	0	4
Q1N4	C^3	14	5	4	0	5
Q1N2.1	C^1	12	4	$1.\bar{6}$	0	2
Q1N2.2	C^1	14	5	1.5	1	2
Q1N2.3	C^1	16	6	1.4	2	2
Q1N3.1	C^2	14	5	2	0	3
Q1N3.2	C^2	16	6	1.8	0	2
Q1N3.3	C^2	18	7	$1.\bar{6}$	1	2

Table 1: Surface continuity, number of degrees of freedom per element, number of surface nodes per element n_s^e, node span, number of basis functions exclusive to one element n_{ex}, and maximum basis support n_{max} for different elements in 2D.

the refinement strategies. Following the k-refinement, t additional steps of p-refinement by means of order elevation are carried out. The order of each element is thus increased to $p+t$, the continuity remains C^{p-1}. To distinguish these elements from the k-refined elements Q1Np, the notation is extended. The number t of additional steps of p-refinement is appended to the element notation of the k-refined element it is based on, Q1N$p.t$. An element that is k-refined to the order 2, followed by one step of additional p-refinement, is thus denoted Q1N2.1. Elements that are only k-refined are also denoted Q1Np.0, but the trailing 0 is dropped for a shorter notation. In Figure 3, elements in one row are of the same order, but the continuity decreases from left to right. The increase of control points on the contact surface and their even distribution over the entire surface compared to k-refinement is advantageous for contact computations.
Some criteria to compare the different Q1N$p.t$ elements besides the continuity across element boundaries are presented in Table 1. The number of surface nodes per element is $n_s^e = p+t+1$ for 2D elements. It is independent of the refinement type and only depends on the order of the basis. The node span is defined as the distance between the outermost control points of an element, measured in the element length L_e for a regular mesh. A large node span implies larger smoothing effects, as changes in distant control points influence the element. One can show that for $t \to \infty$, the node span $\to 1 \quad \forall\ p$. Another property to look at is the number of basis functions whose support lies entirely within one element n_{ex}. These basis functions only influence the one element and consequently allow for very local changes. The last property considered is the maximum basis function support n_{max} in terms of elements. It measures the maximum number of elements that are influenced by one basis function and is an indicator for the amount of smoothing introduced by these elements.

3.4 Numerical integration

The evaluation of the weak form relies on numerical integration, which must be considered adequately for the enriched elements. As with standard finite elements, the integration is performed on a master element with the parametrization ranging from -1 to 1 in each direction. One can distinguish between the volume integrals related to the internal virtual work and the surface integrals related to the virtual contact work. For the latter case, considering a NURBS surface of order p and q in ξ and η direction, respectively, one simply uses $(p+1)(q+1)$ Gauss-Legendre quadrature points in the usual tensor product fashion.
To ensure the stiffness matrix is of full rank in the volume integral, the number of quadrature points needs to be increased with increasing number of control points on the surface. The

simplest way to do this is to use the number of quadrature points required for the highest NURBS order in the tensor product structure, resulting in $(\max(p,q)+1)^3$ quadrature points in $\mathbb{R}^3$. To reduce the computational cost, it is advantageous to define the Gauss-Legendre quadrature points in a tensor product fashion, but with varying number of quadrature points in each direction. Using $(p+1)$ and $(q+1)$ quadrature points in the directions of the NURBS surface and 2 quadrature points in the direction of the linear basis functions, the total number of quadrature points can be reduced to $2(p+1)(q+1)$ quadrature points per enriched element in $\mathbb{R}^3$.
It is most likely possible to derive specialized integration rules for certain enriched elements which achieve the same accuracy with fewer quadrature points, but this is not considered in the scope of this paper.

3.5 Integration into existing code

The integration of the NURBS-enriched elements into an existing finite element analysis code is straightforward and possible with only minor changes. However, some requirements must be fulfilled: The number of nodes per element must be flexible to allow for NURBS of arbitrary order on the surface. This also means that entries in the element connectivity matrix can have different lengths. By using the Bézier extraction operator, the shape function evaluation is identical for each NURBS-enriched element and only requires the evaluation of Bernstein polynomials at the quadrature points. However, in general the localized Bézier extraction operator $\mathbf{C}^e$ must be stored for each element, as shown in equation (16). With the exception of the shape function evaluation, everything remains the same as in the standard case on the quadrature point level, as long as the varying number of shape functions is taken into account. Also, as stated in the previous section on numerical integration, the definition of quadrature rules with varying number of quadrature points in each direction is helpful to increase efficiency. The assembly procedure also remains unchanged, although it is worth noting that the bandwidth of the resulting stiffness matrix is increased due to the larger support of the NURBS basis functions.

3.6 Lagrange and Hermite enrichment

Two enrichment techniques are investigated in [Sauer (2011)], Lagrange and Hermite enrichment. The Lagrange enrichment uses higher-order Lagrangian basis functions on the surface in 2D and 3D. Only the quadratic enrichment Q1C2 is compared to the NURBS enrichment, since high-order Lagrangian interpolation is prone to oscillate.
The Hermite surface enrichment, Q1CH, yields a C^1-continuous surface. This is done by adding degrees of freedom for the surface derivatives on the contact surface. The formulation achieves very good results and is compared to the NURBS enrichment, but it is not available for 3D.

4 Numerical examples

The performance of NURBS-enriched contact elements is illustrated by several numerical examples and compared to standard linear finite elements as well as Hermite and quadratic Lagrange enriched contact elements. In the first example, two-dimensional frictionless ironing, contact leads to local tangential motion between the bodies. In contrast, local motion in normal direction is caused by the adhesive contact forces in the second example, the peeling of an elastic strip. The third example, the delamination of a double cantilever beam, combines both local

normal and tangential motion in the contact zone. The contact-surface enrichment is applied to a three-dimensional example with two deformable bodies in the last example.

4.1 Frictionless ironing

We first consider a deformable half-cylinder $\mathcal{B}_1$ sliding over a deformable block $\mathcal{B}_2$. The problem set-up is taken from [Sauer (2013)], which considered surface enrichments with Q1C2 and Q1CH elements. Initially, the block has the dimensions $10\,L_0 \times 2\,L_0$ and the cylinder a radius of L_0. A vertical displacement of $2/3\,L_0$ is applied to the top of the cylinder, followed by horizontal frictionless sliding, illustrated in Figure 4. The base of the block is fixed and periodic boundary conditions are applied on either end. Contact between the bodies is treated with the penalty method, see equation (5), with $\varepsilon_\mathrm{n} = 1000\,E_0/L_0$. Both bodies use an isotropic, non-linear Neo-Hookean material model [Zienkiewicz and Taylor (2005)]

$$\boldsymbol{\sigma} = \frac{\Lambda}{J}(\ln J)\boldsymbol{I} + \frac{\mu}{J}(\boldsymbol{F}\boldsymbol{F}^T - \boldsymbol{I}) \,, \tag{21}$$

where J is the determinant of the deformation gradient $\boldsymbol{F}$ and $\boldsymbol{I}$ is the identity tensor. The shear modulus $\mu = E/(2(1+\nu))$ and bulk modulus $\Lambda = 2\mu\nu/(1-2\nu)$ are expressed in terms of Young's modulus E and Poisson's ratio ν, which are taken as $E_1 = 3\,E_0$, $E_2 = E_0$ and $\nu_1 = \nu_2 = 0.3$. Parameters L_0 and E_0 are used for normalization of the model. Three nested meshes are considered with 4, 8, and 16 elements per L_0 on the block. The coarsest mesh is shown in Figure 4. The entire upper surface of the block and the curved surface of the cylinder are considered as the contact surface that is enriched.
First, we compare the NURBS-enriched contact elements Q1N2 to standard linear elements Q1C1, quadratic Lagrange enriched elements Q1C2, and Hermite enriched elements Q1CH. During sliding, a non-physical oscillation of the contact force can be observed in both vertical and horizontal direction, illustrated in Figure 5. The horizontal contact force ought to be zero for the frictionless case considered here, and as the depression is fixed during sliding, the vertical contact force should be constant. The two-half-pass contact algorithm described in section 2.1 is used, which evaluates the contact force on each surface separately. This leads to two contact forces, P_1 acting on the half-cylinder and P_2 acting on the block. For the horizontal contact force P_x on the left of Figure 5, the forces $P_{1,x}$ and $P_{2,x}$ are indistinguishable for the enriched contact elements at this scale, the difference is only visible for standard linear elements, for which it is also very small. In vertical direction on the right of Figure 5, the difference between both contact forces is more pronounced for all element types.

The oscillation amplitude of the contact force can be defined in two different ways. The total oscillation amplitude

$$\Delta P = \max(P_1, P_2) - \min(P_1, P_2) \tag{22}$$

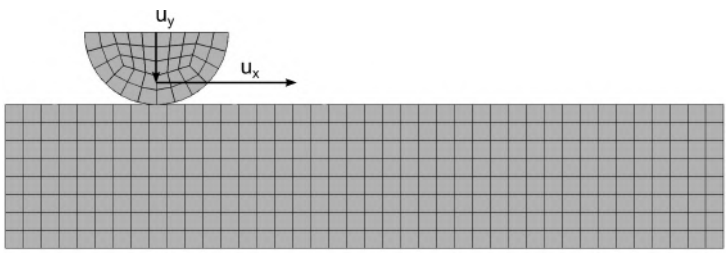

Figure 4: Set-up of the ironing problem.

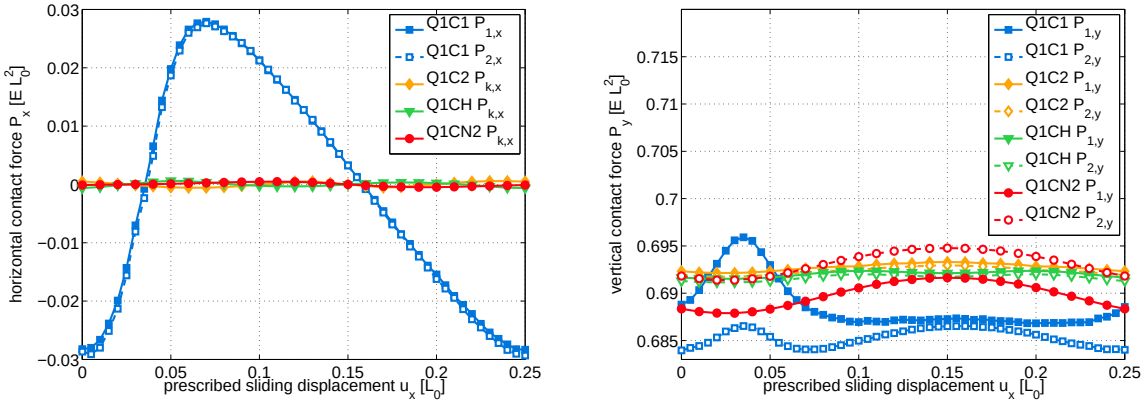

Figure 5: Oscillation of the horizontal and vertical contact force, P_x and P_y respectively, on each body for Q1C1 and surface enrichments Q1C2, Q1CH, and Q1N2 on the coarsest mesh.

measures the difference between the maximum force and the minimum force over both surfaces. Alternatively, the amplitude stemming only from the enriched contact elements without the error induced by the two-half-pass contact algorithm

$$\Delta P_{\text{ece}} = \max\left(\Delta P_1,\, \Delta P_2\right) \tag{23}$$

with $\Delta P_k = \max(P_k) - \min(P_k)$ considers the maximum of the oscillation amplitude of the contact force measured on each surface separately.

The close-up view in Figure 6 shows that while the contact forces remain indistinguishable for Q1C2 and Q1CH elements also at this scale, a small difference in the forces $P_{1,x}$ and $P_{2,x}$ is evident for Q1N2 elements. This is due to the smaller number of degrees of freedom on the surface, which limits the conformity of both surfaces. The possibility of conforming meshes is further limited by the use of different basis functions on both surfaces: while the weights of the control points of the initially flat surface of the block are all 1, effectively reducing the NURBS basis to a B-splines basis, the values of the weights on the cylinder surface vary in order to initially describe an exact half-circle.

With Q1C2 and Q1CH elements, the horizontal contact force oscillation ΔP_x is reduced to 2% of that observed with linear elements. Using Q1N2 elements, ΔP_x is reduced to 1.7%. This reduction is remarkable, considering that the discretization with Q1N2 elements has only two degrees of freedom more than the linear discretization, independent of the mesh refinement. In comparison, the use of Q1C2 elements increases the degrees of freedom by 24 and Q1CH by 26 on the coarsest mesh. The increase of degrees of freedom grows with the number of elements on the surface with the Q1C2 and Q1CH enrichments. In conclusion, the reduction of the oscillation with Q1N2 elements can be attributed to the C^1-continuity of the surface, as the number of degrees of freedom is comparable to linear C^0 elements. The significant improvement provided by a C^1-continuous surface can be seen in the close-up view of the mesh with Q1C1 elements compared to Q1N2 elements during sliding in Figure 7. Non-physical gaps appear between both bodies with linear elements and they interlock during sliding due to the non-smooth surface.

In vertical direction, the two-half-pass algorithm has a greater influence on the results for NURBS enriched elements than on those for other enriched elements. For Q1C2 and Q1CH elements, the oscillation of the vertical contact force oscillation $\Delta P_y \approx \Delta P_{y,\text{ece}}$ is reduced to

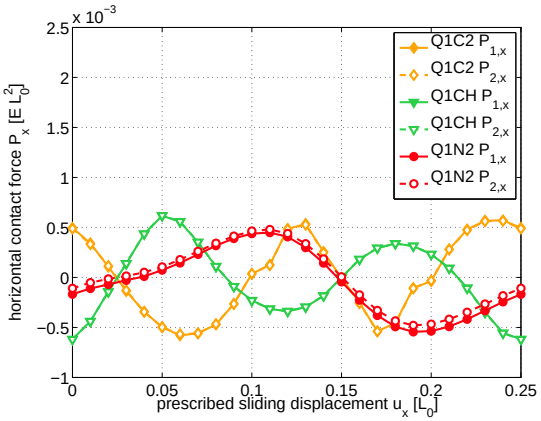

Figure 6: Oscillation of the horizontal contact force P_x on each body for Q1C2, Q1CH, and Q1N2 elements on the coarsest mesh.

13% for Q1C2 and 9% for Q1CH. For Q1N2 elements, the oscillation ΔP_y is reduced only to 58%. Excluding the influence of the contact algorithm, the error $\Delta P_{y,\text{ece}}$ is reduced to 41%. The greater influence of the two-half-pass algorithm is accredited to the limiting factors to conforming meshes discussed above.

Next, the different refinement strategies discussed in section 3.3 and their convergence are examined. Refining the model via k-refinement leads to the element sequence Q1N2, Q1N3, and Q1N4. Recall that this refinement leads to high continuity across element boundaries, basis functions with large support, and node agglomeration at patch edges and points of reduced continuity. Refining the model with the proposed surface oriented approach yields the element sequence Q1N2, Q1N2.1, and Q1N2.2. This refinement strategy leads to a C^1-continuous surface description across all element boundaries on the contact surfaces and results in more degrees of freedom on the contact surface. Note that the appearance of the mesh in terms of element size and geometry is identical for all meshes, merely the continuity and the number of control points changes.

The results of both approaches for the mesh with 8 elements per L_0 are illustrated in Figure 8 for the horizontal contact force and in Table 2 for both force components. One step of the surface-oriented refinement approach already leads to a major reduction of the oscillation to 28.9% and 13.5% in horizontal and vertical direction, respectively, compared to the enriched

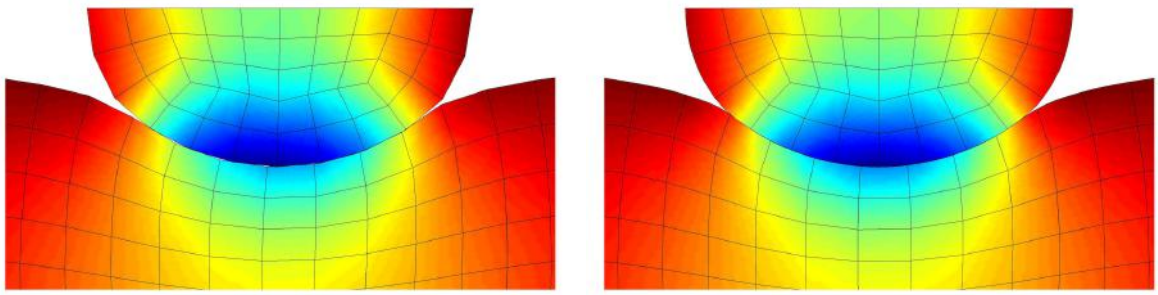

Figure 7: Close up of Q1C1 (left) and Q1N2 (right) mesh during sliding, colored by stress invariant $I_1 = \text{tr}\,(\boldsymbol{\sigma})/E_0$.

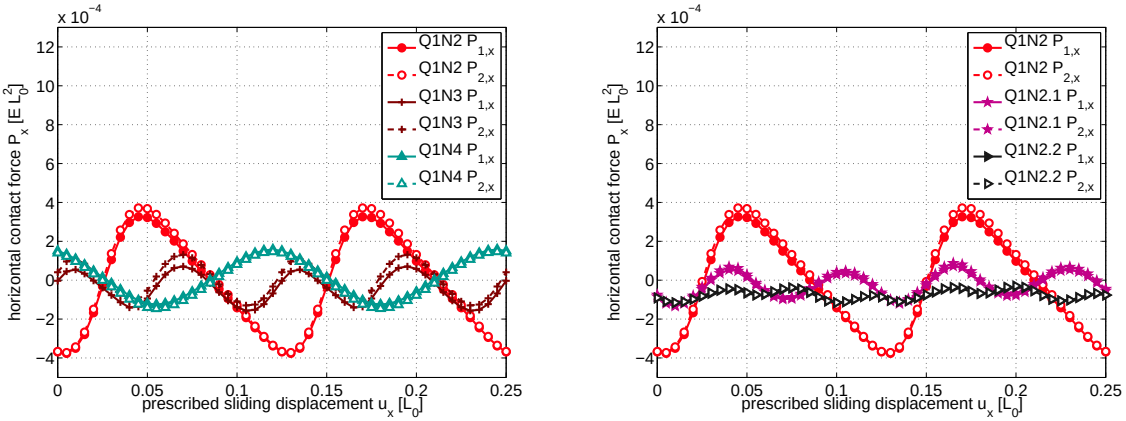

Figure 8: Oscillation of the horizontal contact force on each body for different refinement techniques: k-refinement on the left, surface-oriented refinement on the right.

enrichment	$\Delta P_{x,\text{ece}}$	$\Delta P_{y,\text{ece}}$
Q1N2	100%	100%
Q1N3	35.0%	59.0%
Q1N4	39.0%	47.2%
Q1N2.1	28.9%	13.5%
Q1N2.2	11.5%	11.9%

Table 2: Reduction of the horizontal and vertical contact force oscillation using different refinement techniques.

Q1N2 elements. Not only is the improvement smaller with k-refinement, the horizontal contact force oscillation even increases from Q1N3 to Q1N4. The reason for this is the increasing support of the basis functions with increasing continuity across element boundaries. A sharp contact line cannot be represented by these very smooth basis functions, leading to a smearing of the contact zone. These results motivate the preference of surface-oriented refinement over k-refinement for surface-effect dominated computations.
In addition to the reduction of the oscillation, Figure 8 also illustrates that the error induced by the two-half-pass contact algorithm becomes negligible with increasing refinement for both refinement techniques, as the contact forces on both surfaces become indistinguishable.

Finally, the convergence of the NURBS enriched elements with mesh refinement is considered, using three nested meshes. Figure 9 shows the convergence of the horizontal contact force oscillation amplitude $\Delta P_{x,\text{ece}}$ and the vertical contact force oscillation amplitude $\Delta P_{y,\text{ece}}$, respectively. Both k-refinement and surface-oriented refinement are considered.

For all elements, mesh refinement leads to smaller oscillation amplitudes. Considering $\Delta P_{x,\text{ece}}$ for Q1N4 elements, poor results are achieved with high smoothness in combination with a coarse mesh. This is due to the smeared contact zone, with becomes smaller as we refine the mesh. The surface-oriented refinement again accomplishes better results than k-refinement.

4.2 Peeling of an elastic strip

The second example we consider is the peeling of an elastic, initially flat strip adhering to a flat, rigid surface. The problem set-up, depicted in Figure 10, is taken from [Sauer (2011)].

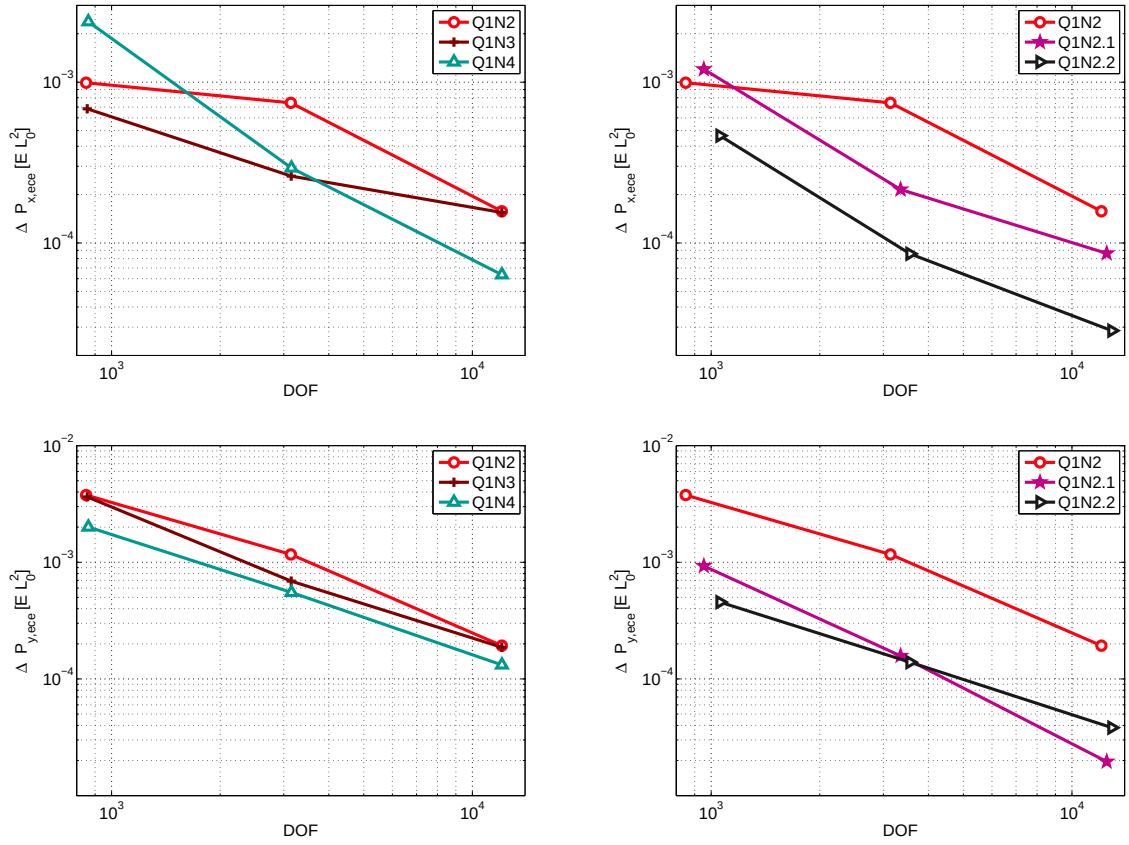

Figure 9: Amplitude of the horizontal contact force $\Delta P_{x,\mathrm{ece}}$ (top) and the vertical contact force $\Delta P_{y,\mathrm{ece}}$ (bottom) for different refinement techniques: k-refinement on the left, surface-oriented refinement on the right.

A rotation Θ is applied at the right boundary, which yields a constant moment during peeling. The strip has the dimensions $200\,L_0 \times 10\,L_0$ and is discretized with 160×8, 240×12, and 320×16 elements. The three discretizations will be referred to as mesh 8, mesh 12, and mesh 16 according to the number of elements over the height. Isotropic, non-linear Neo-Hookean material according to equation (21) with $E = E_0$ and $\nu = 0.2$ is considered. Adhesive van der Waals forces which are described by equation (6) act on 75% of the surface. The parameters $r_0 = 0.4\mathrm{nm}$ and $A_H = 10^{-19}\mathrm{J}$ are chosen as in [Sauer (2011)]. To avoid locking, enhanced assumed strain elements are used in the bulk [Simo and Armero (1992)]. For the enriched elements on the contact surface no such treatment is considered. The influence of one enriched element layer without enhanced strain methods has been shown to not have a significant influence on bending performance [Sauer (2011)]. The deformation of a coarse mesh with 40×2 elements during peeling is illustrated in Figure 11 for Q1N2.1 elements. The elements are colored by

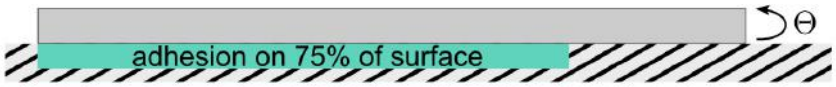

Figure 10: Problem set-up of the peeling example. A rotation Θ is applied at the right boundary.

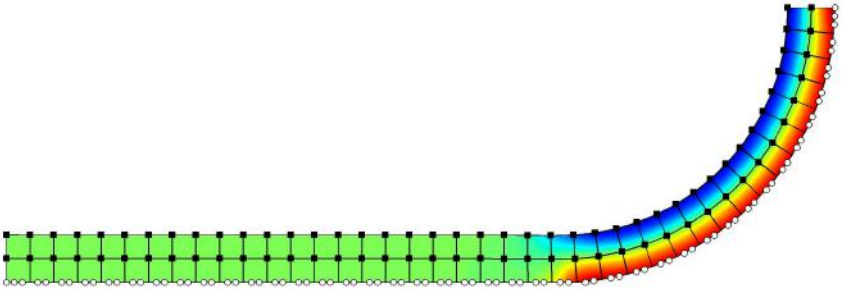

Figure 11: Peeling of an elastic strip at 90°, enriched with Q1N2.1 elements, colored by $I_1 = \mathrm{tr}(\boldsymbol{\sigma})/E_0$. Control points are plotted as white circles, standard finite element nodes as black squares.

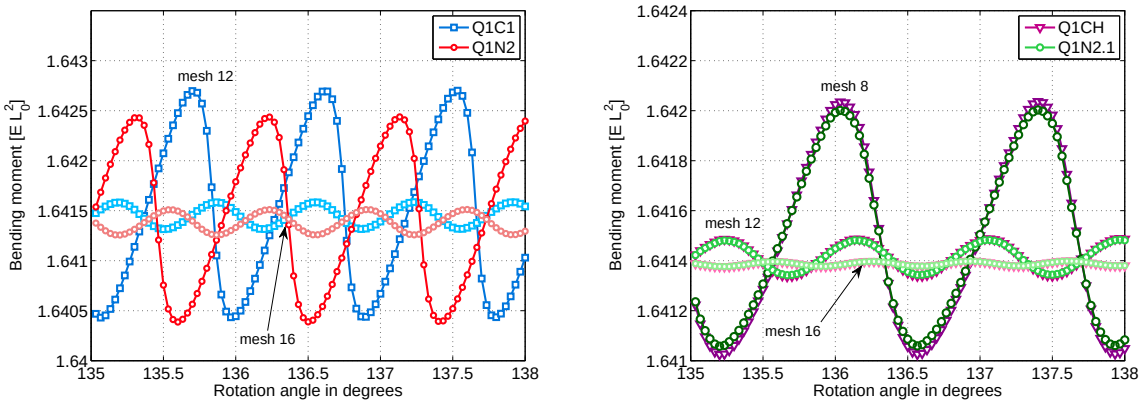

Figure 12: Comparison of the bending moment oscillation.

$I_1 = \mathrm{tr}(\boldsymbol{\sigma})/E_0$ and the control points are plotted as white circles, standard finite element nodes as black squares.

During peeling, the moment at the right boundary of the strip oscillates around a constant value with a wavelength governed by the element length. A reduction not only of the amplitude of the oscillation, but also the steep negative slope which causes difficulties in convergence of the Newton solver is desired. Comparing Q1N2 elements to linear finite elements, the resulting peeling moment only improves slightly, reducing the amplitude to 90% and the negative slope to 80% on mesh 12, see Figure 12 left. The main difference between the Q1N2 and the Q1C1 surface is the C^1-continuity, as the Q1N2 discretization only has two additional degrees of freedom. Hence, the improvement achieved with C^1-continuity is not very large for this problem. Applying one step of order elevation to each Q1N2 element results in Q1N2.1 elements, that reduce the peeling moment oscillation amplitude to 6.3% and the negative slope to 2.5% on mesh 12. These values are slightly better than the results achieved with Hermite enrichment, Q1CH, which reduces the amplitude to 6.7% and the negative slope to 2.6%, see Figure 12 right. In terms of continuity and both degrees of freedom per element and in total, Q1N2.1 and Q1CH are identical, which explains the very similar results.

Refining the mesh, the convergence rate of the oscillation amplitude is the same for all element types. But as Figure 13 shows, the amplitude of the oscillation differs in its absolute value. The Q1C1 and Q1N2 discretizations fail to converge on the coarsest mesh. The figure also illustrates

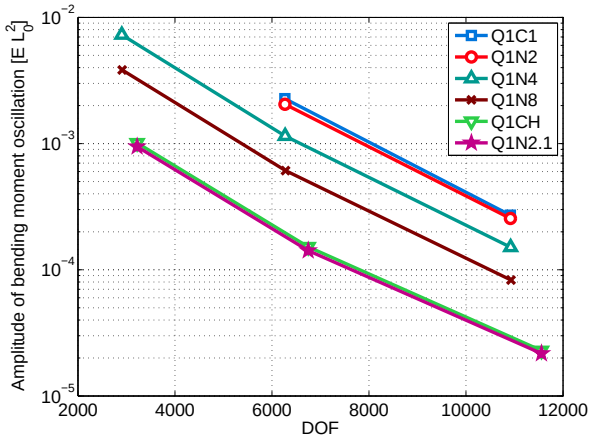

Figure 13: Amplitude of the oscillation of the bending moment for different element types and discretizations.

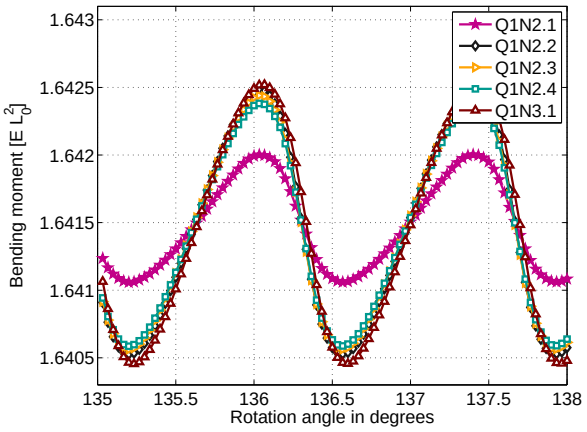

Figure 14: Increase of bending moment oscillation for surface-oriented refinements other than Q1N2.1.

that elements with higher smoothness through k-refinement, Q1N2, Q1N4, and Q1N8, do not decrease the amplitude as well as Q1N2.1 elements with more degrees of freedom on the surface.

An interesting observation is that Q1N2.1 delivers the best results of all tested NURBS enrichments. While other surface-oriented refinements like Q1N2.2 or Q1N3.1 also decrease the oscillation error more than k-refined meshes, they all have a larger amplitude and steeper negative slope than Q1N2.1, see Figure 14. The reason the Q1N2.1 elements outperform the others is subject of ongoing research. A closer look at the control points on the surface and the control polygon they span leads to the observation, that too many degrees of freedom on the surface may be counterproductive for this problem. As depicted in Figure 15, the control points on the surface oscillate with increasing amplitude in the peeling zone with increasing order elevation t. For visibility, the control points of each mesh are shifted by $1\,L_0$ in x-direction and $-0.0015\,L_0$ in y-direction with respect to the previous mesh. The result of the oscillating control points are waves on the surface, which are not as pronounced as in the control polygon due to the variation diminishing property of splines, but affect the accuracy of the computation.

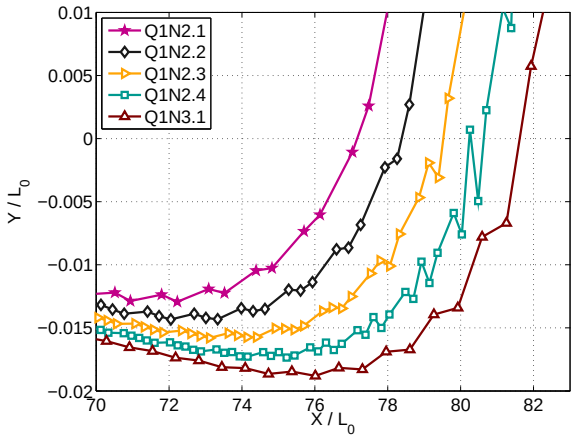

Figure 15: Control polygon for different element enrichments at the peeling front.

4.3 Delamination of a double cantilever beam

The third example considers the debonding of two flexible strips. It is taken from [Sauer (2013)] and the set-up is depicted in Figure 16. Both strips measure $20\,L_0 \times L_0$ and are meshed in a non-conforming manner. A vertical displacement is applied to the upper strip $\mathcal{B}_1$ at the midpoint of its right boundary while the lower strip $\mathcal{B}_2$ is fixed at the midpoint of its right boundary, allowing both strips to rotate around these points. Isotropic, non-linear Neo-Hookean material according to equation (21) is used for both bodies with $E_1 = 3\,E_0$, $E_2 = E_0$, and $\nu_1 = \nu_2 = 0.3$. The strips are bonded along their initially touching surfaces, described by the cohesive zone model in equation (7) with parameters $T_0 = 0.2\,E_0$ and $g_0 = 0.05\,L_0$. No cohesive forces act between the bodies along the part $L_\mathrm{d} = 5\,L_0$ on the right-hand side, which is considered initially debonded. Since penetration is not accounted for in the cohesive zone model (7), an additional quadratic penalty method with penalty parameter $\varepsilon_\mathrm{n} = 50\,E_0/L_0$ is used to prevent penetration. Since the upper strip is three times as stiff as the lower strip, the bonded strips rotate during peeling, shown in Figure 17. This leads to a mixture of locally normal and tangential motion in the debonding zone.

Using linear elements, a non-physical oscillation of the peeling force is observed during delamination, see Figure 18. Considering the k-refined elements Q1N2, Q1N3, and Q1N4, a slight reduction of the oscillation is achieved, see Figure 18 left. Using the surface-oriented refinement technique, Q1N2.1, Q1N2.2, and Q1N3.1, the oscillation is reduced significantly. The oscillation amplitudes are given as percentage of the amplitude of Q1C1 elements in Table 3, including the results obtained with Q1C2 and Q1CH elements.
Like in the previous peeling example in section 4.2, Q1N2.1 and Q1CH yield very similar re-

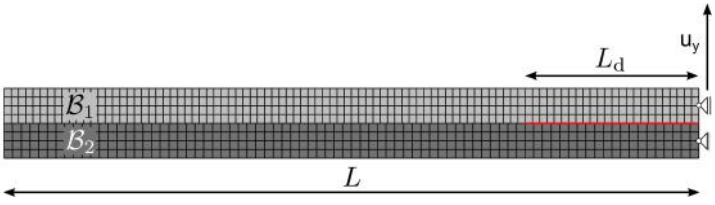

Figure 16: Double cantilever beam problem set-up

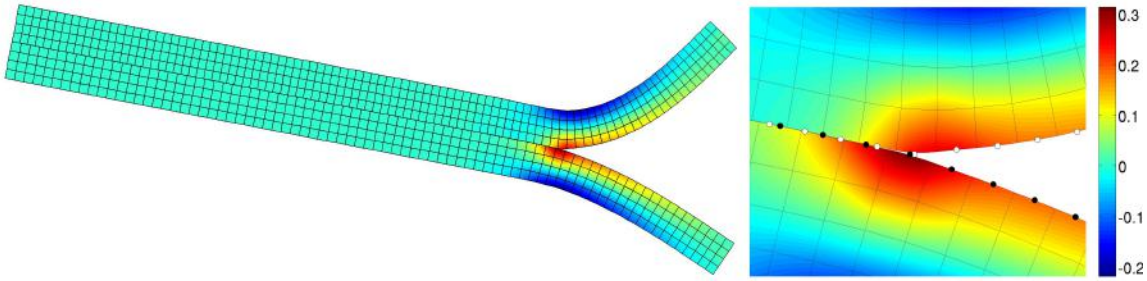

Figure 17: Deformation of the double cantilever beam problem with Q1N2 elements at the onset of debonding, colored by $I_1 = \mathrm{tr}(\boldsymbol{\sigma})/E_0$. In the close-up, the control points are plotted as white and black circles for $\mathcal{B}_1$ and $\mathcal{B}_2$, respectively.

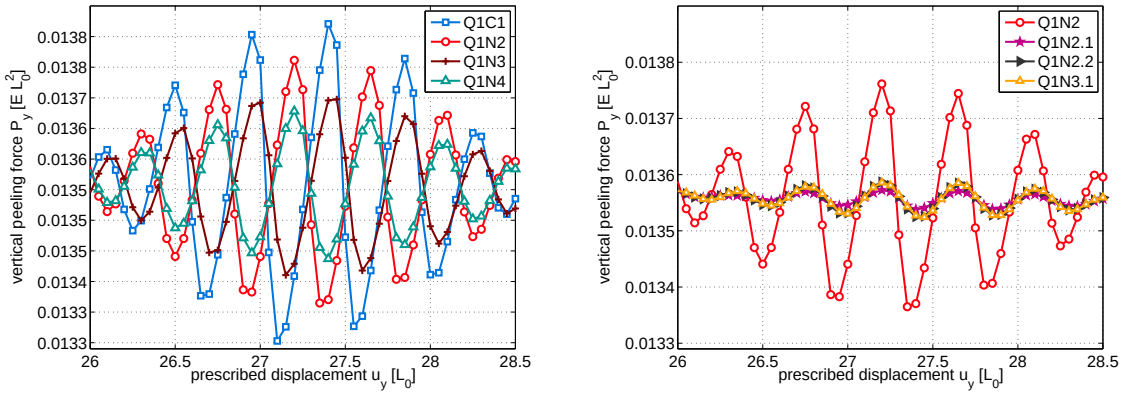

Figure 18: Oscillation in peeling force for different refinement techniques.

sults for the oscillation of the force. The maximum difference in the peeling force between both enrichments is four orders of magnitude smaller than the value of the force. Also, the refinement Q1N2.1 plays a special role again, as the oscillation amplitudes increase for other surface-oriented refinements. Nevertheless, the reduction of the oscillation to 11.9% is still better than the results achieved with k-refined surfaces.

4.4 Three-dimensional twisting

In this example, the surface enrichment is applied to a three-dimensional problem. A cube of size $2\,L_0 \times 2\,L_0 \times 2\,L_0$ is fixed on its lower surface such that it can expand around the midpoint, but rotation around and movement in direction of the vertical axis are restricted. A hollow hemisphere with an outer radius of $R = L_0$ and a wall-thickness of $1/3\,L_0$ is centered above the cube. First, a frictionless downward displacement of L_0 is applied to all nodes on the ring formed by the upper surface of the hemisphere, followed by a frictionless rotation of 90° around the vertical axis. Three meshes are considered, discretizing the cube with 2^3, 4^3, and 8^3 elements and the hemisphere with 3^2, 7^2, and 11^2 elements over the curved surface, and 1, 2, and 3 elements in radial direction. The initial mesh is created using Q1N2 elements on the contact surfaces. To compare it to linear elements, the corner points of the Q1N2 elements are used as nodes for the linear mesh. The contact algorithms implemented for NURBS-enriched elements can also be used directly for linear elements by expressing them as Q1N1 elements with

Enrichment	Oscillation amplitude
Q1C1	100.0%
Q1N2	76.6%
Q1N3	55.4%
Q1N4	46.6%
Q1N2.2	11.9%
Q1N3.1	11.9%
Q1CH	6.7%
Q1N2.1	6.6%

Table 3: Peeling force oscillation amplitude for different enrichments and refinement techniques compared to linear elements.

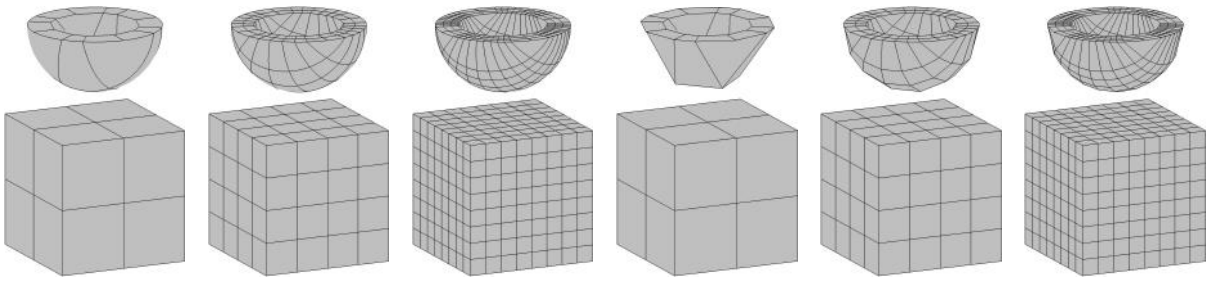

Figure 19: Discretization of the geometry with Q1N2 on the left, Q1N1=Q1C1 on the right.

all weights set to one, which yield identical basis functions to Q1C1 elements. The NURBS-enriched and linear meshes are depicted in Figure 19, where the hemisphere has been elevated for better visualization. Four elements on the hemisphere are degenerated to triangles. As the displacement of the degenerated edges is prescribed by the boundary conditions, they have no negative impact on the results. Creating the hemisphere with these degenerated elements allows for an entirely C^1-continuous surface with Q1N2 elements.

Neo-Hookean material according to equation (21) is used for both bodies, with $E_{\text{cube}} = E_0$, $E_{\text{sphere}} = 5\,E_0$, and $\nu_{\text{cube}} = \nu_{\text{sphere}} = 0.3$. Contact is modeled with the penalty method, equation (5), with penalty parameter $\varepsilon_{\text{n}} = 100\,E_0/L_0$. The problem set-up is illustrated in Figure 20, where a quarter of the block and half the hemisphere have been cut to reveal the internal mesh and stress state. It also allows a better view of the surface deformation. The deformed meshes are colored by $I_1 = \text{tr}\,(\boldsymbol{\sigma})/E_0$.

All three components of the contact force exhibit non-physical oscillations during rotation of the hemisphere. The vertical contact force, that should remain constant, and the torque around the rotation axis, that should be zero, are analyzed. Their deviations are summarized in Table 4 for Q1N2 and Q1C1 elements. The error in the vertical contact force ΔP_z is calculated according to equation (22) while the maximum deviation from zero is taken as measure for the error of the torque around the rotation axis. NURBS-enriched elements outperform linear elements by a factor of 7.5, 2.0, and 1.2 for increasing mesh refinements regarding the vertical contact force. The torque around the rotation axis is improved by factors of 28.5, 5.1, and 4.5 for increasing mesh refinements. In this example, results achieved with Q1N2 elements are of comparable accuracy to the results achieved with the next finer linear mesh.

The deformed contact surfaces and the contact pressure acting on them are shown in Figure

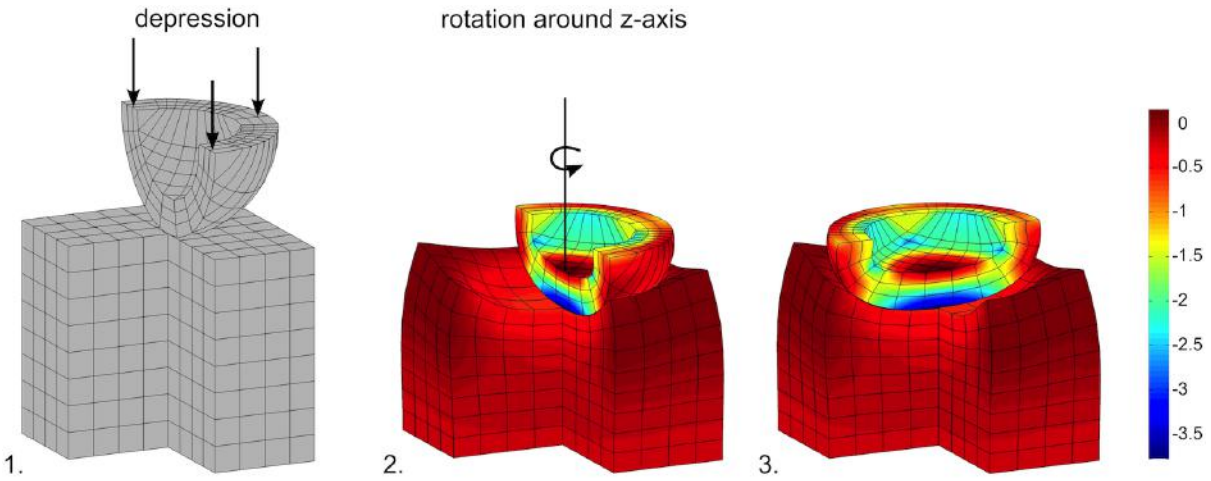

Figure 20: Twisting problem set-up, cut to show internal mesh: 1. Initial geometry 2. Geometry after depression 3. Geometry after rotation by 90°. The deformed meshes are colored by $I_1 = \mathrm{tr}\,(\boldsymbol{\sigma})/E_0$.

mesh	ΔP_z		max(abs(M_z))	
	Q1N2	Q1C1	Q1N2	Q1C1
2	7.778 x 10^{-2}	5.822 x 10^{-1}	8.665 x 10^{-3}	2.469 x 10^{-1}
4	3.125 x 10^{-2}	6.211 x 10^{-2}	3.319 x 10^{-3}	1.698 x 10^{-2}
8	1.896 x 10^{-2}	2.338 x 10^{-2}	7.566 x 10^{-4}	3.409 x 10^{-3}

Table 4: Maximum oscillation errors in P_z normalized by EL_0^2 and maximum deviation of torque M_z from zero normalized by EL_0^3 during rotation for different element types and meshes.

21 for Q1N2 and Q1C1 elements, as well as for a reference solution with Q1N2 elements on a fine grid. For visibility, the contact surface of the hemisphere is elevated. The contact pressure is computed with the post-processing scheme proposed in [Sauer (2013)], which smooths the contact pressure using the finite element interpolation. Considering the contact pressure, the higher degree of smoothing for Q1N2 elements compared to for Q1C1 elements is visible. This is due to the C^1 continuity of the interpolation which is also used for smoothing. Compared to the reference computation, both NURBS enriched and linear elements deliver satisfactory results for the contact pressure. Concerning the deformation of the contact surfaces, the Q1N2 elements are able to capture it more accurately than linear elements.

Considering the efficiency of the formulation, it is obvious that the evaluation of a Q1N2 element with 39 degrees of freedom is computationally more expensive than the evaluation of a tri-linear element with 24 degrees of freedom, or 27 and 12 degrees of freedom on the surface, respectively. However, the use of a smooth C^1 surface description leads to a reduction of the number of Newton iteration steps needed for convergence. For increasing mesh refinements 2, 4, and 8, the maximum number of Newton steps needed for one load-step are 14, 13, and 20 for linear elements, and 8, 7, and 6 for Q1N2 elements. Mesh-refinement reduces the necessary number of Newton iterations for the NURBS-enriched elements while no trend is observed for Q1C1 elements. Independent of mesh-refinement, the problem of interlocking elements remains at a smaller scale for linear elements. The considerable reduction of Newton iteration steps due to the faster convergence leads to a reduction of the runtime with Q1N2 elements by 35% compared to linear elements. As noted above, the code used for the comparison is identical, using Q1N1 elements for the linear case.

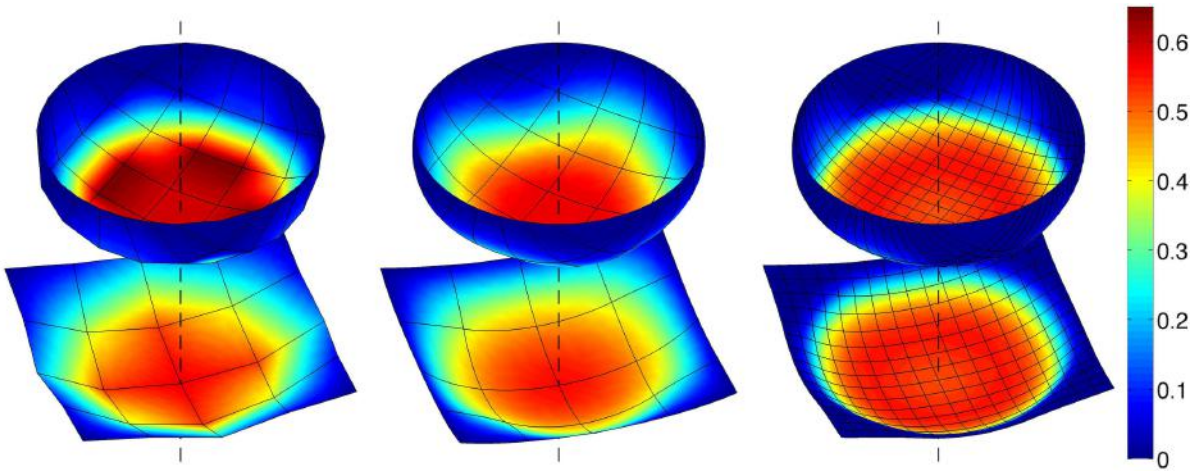

Figure 21: Post-processed contact pressure for Q1C1 (left) and Q1N2 (middle) compared to fine reference solution (Q1N2, right). The elements are colored by the contact pressure normalized by E_0.

5 Conclusion

The novel surface enrichment formulation based on isogeometric analysis presented in this work improves the accuracy of contact computations, even increasing efficiency in some cases. It combines an at least C^1-continuous surface description with high-order surface integral evaluation. Improved accuracy of the deformation and contact forces are achieved for both two-dimensional and three-dimensional contact problems with deformable solids. The evaluation of an enriched contact element comes at a higher computational cost than that of linear elements, but in general only a small number of elements are enriched maintaining efficient linear elements for the vast majority of the domain. Additionally, it is shown that the improved performance of the enrichment is able to reduce the number of Newton iterations necessary for convergence, reducing the overall runtime of the analysis.
Several extension are planned for future work. Frictional contact problems are expected to benefit greatly from the smoothness of the surface and high accuracy of the contact integral evaluation. Also the use of T-splines rather than NURBS will be considered, offering the possibility of local mesh refinement. The development of adaptive mesh enrichment techniques is a possibility to further increase the efficiency of the presented formulation. Finally, the proposed enrichment technique is believed to not only improve contact computations, but could also be used for other surface-effect dominated applications. Examples could include flow problems around deformable solids leading to fluid-structure interaction problems, free surface flows, or electrostatic or electromagnetic interaction.

Acknowledgements

The authors are grateful to the German Research Foundation (DFG) for supporting this research through projects SA1822/5-1 and GSC 111. We also thank Robert Taylor and Thomas Hughes for their helpful comments.

References

Bazilevs, Y., Calo, V. M., Cottrell, J. A., Evans, J. A., Hughes, T. J. R., Lipton, S., Scott, M. A., and Sederberg, T. W. (2010). Isogeometric analysis using T-splines. *Comput. Meth. Appl. Mech. Engrg.*, **199**:229–263.

Borden, M. J., Scott, M. A., Evans, J. A., and Hughes, T. J. R. (2011). Isogeometric finite element data structures based on bezier extraction of NURBS. *Int. J. Numer. Meth. Engng.*, **87**:15–47.

Cottrell, J. A., Hughes, T. J. R., and Bazilevs, Y. (2009). *Isogeometric Analysis*. Wiley.

De Lorenzis, L., Temizer, I., Wriggers, P., and Zavarise, G. (2011). A large deformation frictional contact formulation using NURBS-based isogeometric analysis. *Int. J. Numer. Meth. Engng.*, **87**:1278–1300.

De Lorenzis, L., Wriggers, P., and Zavarise, G. (2012). A mortar formulation for 3D large deformation contact using NURBS-based isogeometric analysis and the augmented Lagrangian method. *Comp. Mech.*, **49**:1–20.

El-Abbasi, N., Meguid, S. A., and Czekanski, A. (2001). On the modeling of smooth contact surfaces using cubic splines. *Int. J. Numer. Meth. Engng.*, **50**:953–967.

Gordon, W. J. and Charles, C. A. (1973). Transfinite element methods: Blending-function interpolation over arbitrary curved element domains. *Numer. Math.*, **21**(2):109–129.

Hughes, T., Cottrell, J., and Bazilevs, Y. (2005). Isogeometric analysis: CAD, finite elements, NURBS, exact geometry and mesh refinement. *Comp. Meth. Appl. Mech. Engrg.*, **194**:4135–4195.

Krstulovic-Opara, L., Wriggers, P., and Korelc, J. (2002). A C^1-continuous formulation for 3D finite deformation friction contact. *Comp. Mech.*, **29**:27–42.

Laursen, T. A. (2002). *Computational Contact and Impact Mechanics: Fundamentals of modeling interfacial phenomena in nonlinear finite element analysis*. Springer.

Lu, J. (2011). Isogeometric contact analysis: Geometric basis and formulation for frictionless contact. *Comput. Methods Appl. Mech. Engrg.*, **200**(5-8):726–741.

Padmanabhan, V. and Laursen, T. A. (2001). A framework for development of surface smoothing procedures in large deformation frictional contact analysis. *Finite Elem. Anal. Des.*, **37**:173–198.

Piegl, L. A. and Tiller, W. (1997). *The NURBS Book*. Springer, 2nd edition.

Sauer, R. A. (2011). Enriched contact finite elements for stable peeling computations. *Int. J. Numer. Meth. Engrg.*, **87**:593–616.

Sauer, R. A. (2013). Local finite element enrichment strategies for 2D contact computations and a corresponding postprocessing scheme. *Comput. Mech.*, **52**:301–319.

Sauer, R. A. and De Lorenzis, L. (2013). A computational contact formulation based on surface potentials. *Comput. Methods Appl. Mech. Engrg.*, **253**:369–395.

Scott, L. R. (1973). *Finite element techniques for curved boundaries*. PhD thesis, Massachusetts Institute of Technology, Cambridge, USA.

Sevilla, R., Fernández-Méndez, S., and Huerta, A. (2008). NURBS-enhanced finite element method (nefem). *Int. J. Numer. Meth. Engng.*, **76**(1):56–83.

Simo, J. C. and Armero, F. (1992). Geometrically non-linear enhanced strain mixed methods and the method of incompatible modes. *Int. J. Numer. Meth. Engng.*, **33**:1413–1449.

Stadler, M. and Holzapfel, G. A. (2004). Subdivision schemes for smooth contact surfaces of arbitrary mesh topology in 3D. *Int. J. Numer. Meth. Engng.*, **60**:1161–1195.

Stadler, M., Holzapfel, G. A., and Korelc, J. (2003). C^n continuous modelling of smooth contact surfaces using NURBS and application to 2D problems. *Int. J. Numer. Meth. Engng.*, **57**:2177–2203.

Temizer, I., Wriggers, P., and Hughes, T. J. R. (2012). Three-dimensional mortar-based frictional contact treatment in isogeometric analysis with NURBS. *Comput. Methods Appl. Mech. Engrg.*, **209-212**:115–128.

Wriggers, P. (2006). *Computational Contact Mechanics*. Springer, 2$^{\text{nd}}$ edition.

Xu, X.-P. and Needleman, A. (1993). Void nucleation by inclusion debonding in a crystal matrix. *Model. Simul. Mater. Sci. Engng.*, **1**(2):111–132.

Zienkiewicz, O. C. and Taylor, R. L. (2005). *The Finite Element Method for Solid and Structural Mechanics*. Butterworth-Heinemann, 6$^{\text{th}}$ edition.

Zlámal, M. (1973). Curved elements in the finite element method. i. *SIAM J. Numer. Anal.*, **10**(1):229–240.